Isospin constraints on the parametric coupling model for nuclear matter

Guilherme F. Marranghello,[1,*] Constança Providência,[2] and Alexandre M. S. Santos[2]
[1]*Centro de Ciências Exatas e Tecnológicas, Universidade Federal do Pampa, Bagé, CEP 96400-970 RS, Brazil*
[2]*Centro de Física Computacional, Department of Physics, University of Coimbra, P-3004-516 Coimbra, Portugal*
(Received 14 November 2009; published 8 February 2010)

We make use of isospin constraints to study the parametric coupling model and the properties of asymmetric nuclear matter. Besides the usual constraints for nuclear matter—the effective nucleon mass and the incompressibility at saturation density—and the neutron star constraints—maximum mass and radius—we study the properties related to the symmetry energy. These properties constrain the parameters of the model to a small range. We apply our results to study thermodynamic instabilities in the liquid-gas phase transition as well as neutron star configurations.

DOI: 10.1103/PhysRevC.81.024307 PACS number(s): 21.65.Ef, 24.10.Jv, 26.60.Kp, 21.65.Cd

I. INTRODUCTION

The search for an effective nuclear matter theory has been one of the main goals of nuclear physics (see, e.g., the pioneering work of Fetter and Walecka [1]). The advances in experimental data acquisition have played an essential role in the improvement of nuclear models. One of the most required parameters to constrain symmetric nuclear matter models, the incompressibility [2], has made many contributions since the nonlinear Boguta and Bodmer model [3] was proposed as an alternative to the Walecka model [4]. The derivative coupling models proposed by Zimanyi and Moszkowski (ZM) were also inspired to correct distortions in the incompressibility and effective nucleon mass determinations [5].

In this work we make use of the so-called parametric coupling model (PCM) [6], which describes nuclear matter with density-dependent coupling constants. The PCM, presented in Sec. II, has appeared in the literature since the first attempt to unify Walecka and ZM models in a unique model [7]. The PCM was successful in reproducing the results obtained in the Walecka [4], ZM [5], and exponential coupling models [8] and even more successful in reproducing nuclear matter and neutron star main properties using special choices for the free parameters that define the density dependence of the coupling constants. The PCM has been used to study a wide range of problems, especially the nuclear matter compression modulus [9], the inclusion of strange meson fields [10], and the hadron-quark phase transition [11,12].

Presently, an important issue in nuclear physics is to constrain the nuclear matter equation of state (EOS) from compact star properties or from laboratory measurements such as those planned for the next generation of exotic radioactive beam facilities at CSR, China, FAIR, Germany, RIKEN, Japan, and SPIRAL2(GANIL), France, or the planned Facility of Rare Isotope Beams, USA, where the high-density behavior of symmetry energy will be further studied experimentally. While saturation properties of symmetric nuclear matter such as the saturation density, binding energy, and incompressibility are quite well settled, properties of asymmetric nuclear matter, such as the density dependence of the symmetry energy, are much less constrained.

Many authors have recently tested nuclear models, phenomenological [13–23], variational [17], and microscopic [18,24], such as the Brueckner-Hartree-Fock formalism, to impose constraints or verify their compatibility with data coming from heavy-ion collisions (HICs), giant monopole resonances, or isobaric analog states. In particular, recent experimental constraints from isospin diffusion in HICs gave the values $L = 88 \pm 25$ MeV for the slope parameter of the symmetry energy and $K_\tau = -500 \pm 50$ MeV for the isospin incompressibility coefficient [16,18]. The latter is in agreement with the value of $K_\tau = -550 \pm 100$ MeV predicted by the independent measurement of the isotopic dependence of the giant monopole resonance in Sn isotopes [25,26] and the value of $K_\tau = -500^{+125}_{-100}$ MeV obtained from the study of neutron skins [19]. On the contrary, isoscaling in HICs favors $L \sim 65$ MeV [27] and nucleon emission ratios favor $L \sim 55$ MeV [28].

The main goal of the present work is to constrain even more the free parameters in the PCM by studying the symmetry energy and its density dependence through its slope and its second derivative with respect to the density. We try to establish some correlations between the symmetry energy, and its density derivatives, and quantities of astrophysical interest such as the crust-core crossing density, the density at muon and at strangeness onset, the maximum star mass, and the threshold star mass for direct Urca [29].

We summarize the PCM in Sec. II and discuss the symmetry energy dependence on the density in Sec. III, the thermodynamic instabilities in Sec. IV, and the neutron star properties in Sec. V. Finally, we draw some conclusions in Sec. VI.

II. PARAMETRIC COUPLING MODEL

We first study the nuclear matter properties within the PCM. This model is based on the Walecka model [4]. However, to correct the values of the effective nucleon mass and incompressibility of symmetric nuclear matter at saturation density, Taurines *et al.* [6] have introduced parametric couplings. They are introduced in a manner similar to that used by ZM to

*gfmarranghello@gmail.com

include the derivative couplings in their models. Here we briefly describe the model and the reader is referred to Ref. [6] for further details. The PCM Lagrangian density reads

$$\mathcal{L} = \sum_B \bar{\psi}_B[i\gamma_\mu\partial^\mu - (M_B - g^\star_{\sigma B}\sigma) - g^\star_{\omega B}\gamma_\mu\omega^\mu]\psi_B - \sum_B \psi_B\left[\frac{1}{2}g^\star_{\rho B}\gamma_\mu\tau\cdot\rho^\mu\right]\psi_B + \sum_\lambda \bar{\psi}_\lambda[i\gamma_\mu\partial^\mu - m_\lambda]\psi_\lambda + \frac{1}{2}(\partial_\mu\sigma\partial^\mu\sigma - {m_\sigma}^2\sigma^2) - \frac{1}{4}\omega_{\mu\nu}\omega^{\mu\nu} + \frac{1}{2}{m_\omega}^2\omega_\mu\omega^\mu - \frac{1}{4}\rho_{\mu\nu}\cdot\rho^{\mu\nu} + \frac{1}{2}m_\rho^2\rho_\mu\cdot\rho^\mu, \quad (1)$$

where

$$g^\star_{\sigma B} \equiv m^\star_{\alpha B}g_\sigma, \quad g^\star_{\omega B} \equiv m^\star_{\beta B}g_\omega, \quad g^\star_{\rho B} = m^\star_{\gamma B}g_\rho, \quad (2)$$

and

$$m^\star_{nB} \equiv \left(1 + \frac{g_\sigma\sigma}{nM_B}\right)^{-n}, \quad n = \alpha, \beta, \gamma\,. \quad (3)$$

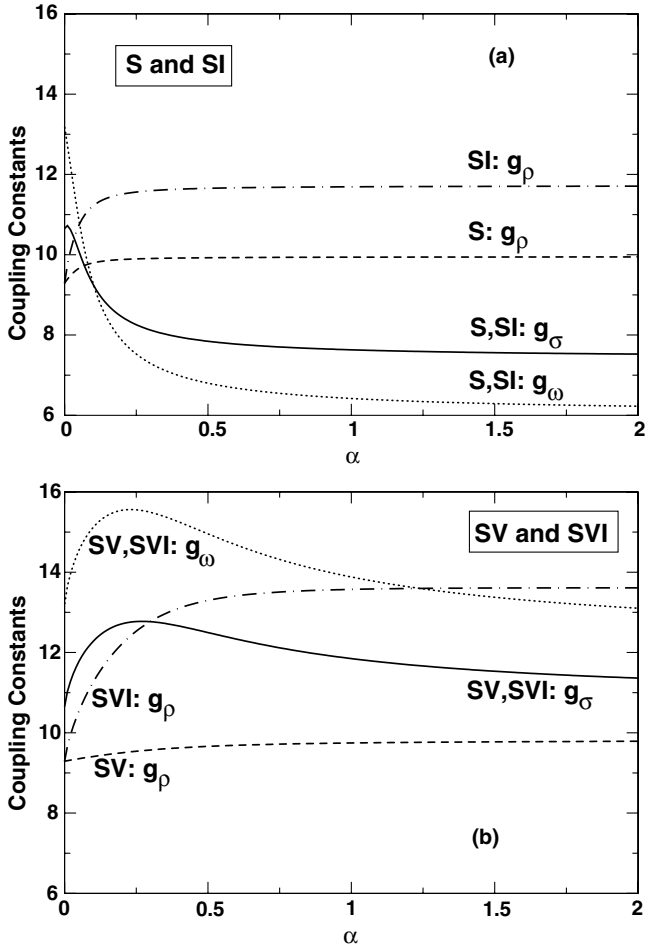

FIG. 1. Coupling parameters g_i of models (a) S and SI and (b) SV and SVI, as a function of α. For each pair of models the g_σ and g_ω parameters are equal and only the g_ρ couplings vary: g_σ (solid line), g_ω (dotted line), and g_ρ (dashed line for S and SV; dot-dashed line for SI).

In the preceding equations, ψ_B represents the baryon fields that can be summed over the whole baryon octet. The baryon fields are coupled to the meson fields σ, ω, and ρ. The electron and muon fields appear as ψ_λ and must be introduced for the description of stellar matter.

The parametric couplings restore the Walecka model for $\alpha = \beta = \gamma = 0$, the ZM1 model for $\alpha = 1$ and $\beta = \gamma = 0$, the ZM3 model for $\alpha = \beta = 1$ and $\gamma = 0$, and the exponential coupling model for $\alpha = \beta = \gamma = \infty$. The g_σ and g_ω coupling constants are chosen to reproduce the binding energy $E_B = \epsilon/\rho - M = -15.75$ MeV at the saturation density $\rho_0 = 0.16$ fm^{-3}. We fix the isovector coupling constant g_ρ to fit the symmetry energy $a_4 = 32.5$ MeV, at the same saturation density.

We work with four versions of the PCM: (a) varying the scalar parameter α with the vector parameter $\beta = 0$ and isovector parameter $\gamma = 0$ (model S); (b) varying the scalar and vector parameters $\alpha = \beta$ while keeping the isovector parameter $\gamma = 0$ (model SV); (c) varying all three parameters, $\alpha = \beta = \gamma$ (model SVI); and (d) varying the scalar and isovector parameters $\alpha = \gamma$ while keeping the vector parameter $\beta = 0$ (model SI). We expect to verify the dependence of the nuclear matter main properties on the coupling constants. We also consider the parametrization (a) SI2, with $\alpha = 0.1$, $\beta = 0$, and (b) SVI2 $\alpha = \beta = 0.2$, while, in both cases, we vary γ. The latter two choices allow us to explore the isovector degree of freedom while choosing reasonable properties for the isoscalar channel, namely, for symmetric nuclear matter.

In Fig. 1, we present the meson couplings g_σ, g_ω, and g_ρ, as a function of the parameter α for all models. We plot the couplings for models S and SI in Fig. 1(a) and those for models SV and SVI in Fig. 1(b). Because the values of the g_σ and g_ω couplings are first chosen to reproduce symmetric nuclear matter data, and only after this choice is the value of

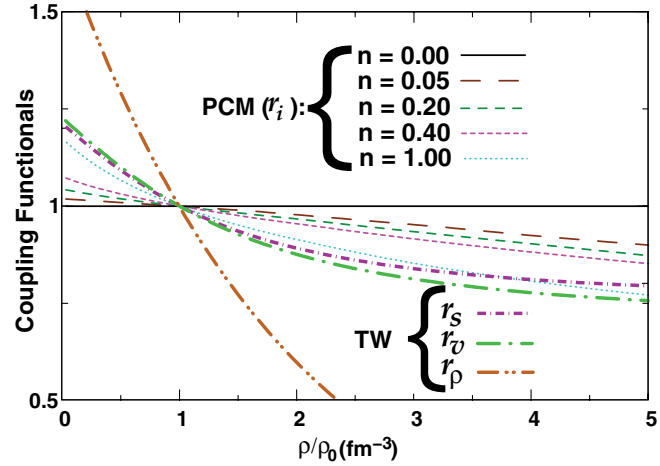

FIG. 2. (Color online) Effective-to-bare coupling constant ratio g_i^*/g_i for $n = 0.0$ (solid line), 0.05 [(brown) long-dashed line], 0.20 [(dark-green) medium-dashed line], 0.40 [(pink) short-dashed line], and 1.0 [(cyan) dotted line] with $i = \sigma, \omega, \rho$ for different choices of α in the PCM, as well as TW functionals r_σ [(purple) short-dot-dashed line], r_ω [(light-green) long-dot-dashed line], and r_ρ [(light-brown) dot-dot-dashed line], where $r_i = \Gamma_i/\Gamma_0$. Note that TW curves are shown with thicker lines.

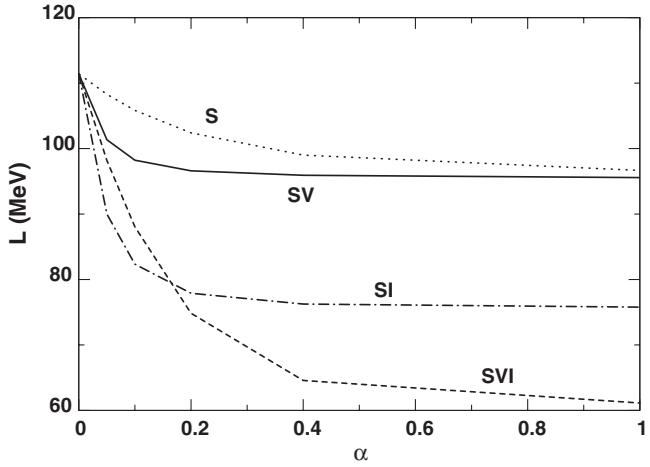

FIG. 3. Dependence of the slope of symmetry energy on the free parameter α for models S (dotted line), SV (solid line), SI (dot-dashed line), and SVI (dashed line).

g_ρ established, the scalar and vector coupling constants are the same for the pairs of models S/SI and SV/SVI. These two pairs of models differ only in the isovector channel. It is shown that for models S and SI the g_ρ parameter has stabilized at a constant value of $\alpha \sim 0.2$. For models SV and SVI this occurs only for $\alpha \sim 0.5$. The g_σ and g_ω parameters stabilize only for $\alpha \sim 1$, however, saturation properties of symmetric nuclear matter restrict the accepted values to $\alpha < 1$. In all four versions of the model, $\alpha = \infty$ has a stable result that essentially does not differ from $\alpha = 2$ and the changes from $\alpha = 1$ are very small. The density dependence of the coupling constants can be examined in Fig. 2, where we have plotted $\frac{g_i^*}{g_i} = m_n^* = (1 + \frac{g_\sigma \sigma}{nM_B})^{-n}$.

The greater the value of n, the stronger the density dependence and the reduction of the effective coupling constant value at higher densities. To compare the results obtained with the PCM, we have also plotted in Fig. 2 the density dependence of the relative Typel and Wolter (TW) couplings [30]. The behavior of Γ_i/Γ_{i0}, $i = \sigma$, ω, is similar to that obtained with the PCM for $\alpha = 1$. The same does not occur for Γ_ρ, which has a much faster decrease with density.

We have included hyperons in the present model for the high-density EOS in the inner regions of a neutron star. Because discussion of the hyperon coupling constants is not the aim of this work, we just fix the hyperon-meson coupling constants to $\chi = \frac{g_{\sigma Y}}{g_{\sigma N}} = \frac{g_{\omega Y}}{g_{\omega N}} = \frac{g_{\rho Y}}{g_{\rho N}} = \sqrt{2/3}$. To study neutron stars we must also include the Baym-Pethick-Sutherland (BPS) EOS for densities below the neutron drip line [31].

III. SYMMETRY ENERGY

In Tables I–IV we report some of the properties of the models under study: the symmetry energy slope $L = 3\rho_0 \partial E_{\rm sym}/\partial\rho$, the symmetry energy incompressibility $K_{\rm sym} = 9\rho_0^2 \partial^2 E_{\rm sym}/\partial\rho^2$, the symmetry term of the incompressibility of the nuclear EOS $K_\tau = K_{\rm sym} - L(6 - Q_0/K)$, where $Q_0 = 27\rho_0^3 \partial^3(E/A)/\partial\rho^3$, the effective nucleon mass M^*/M, the

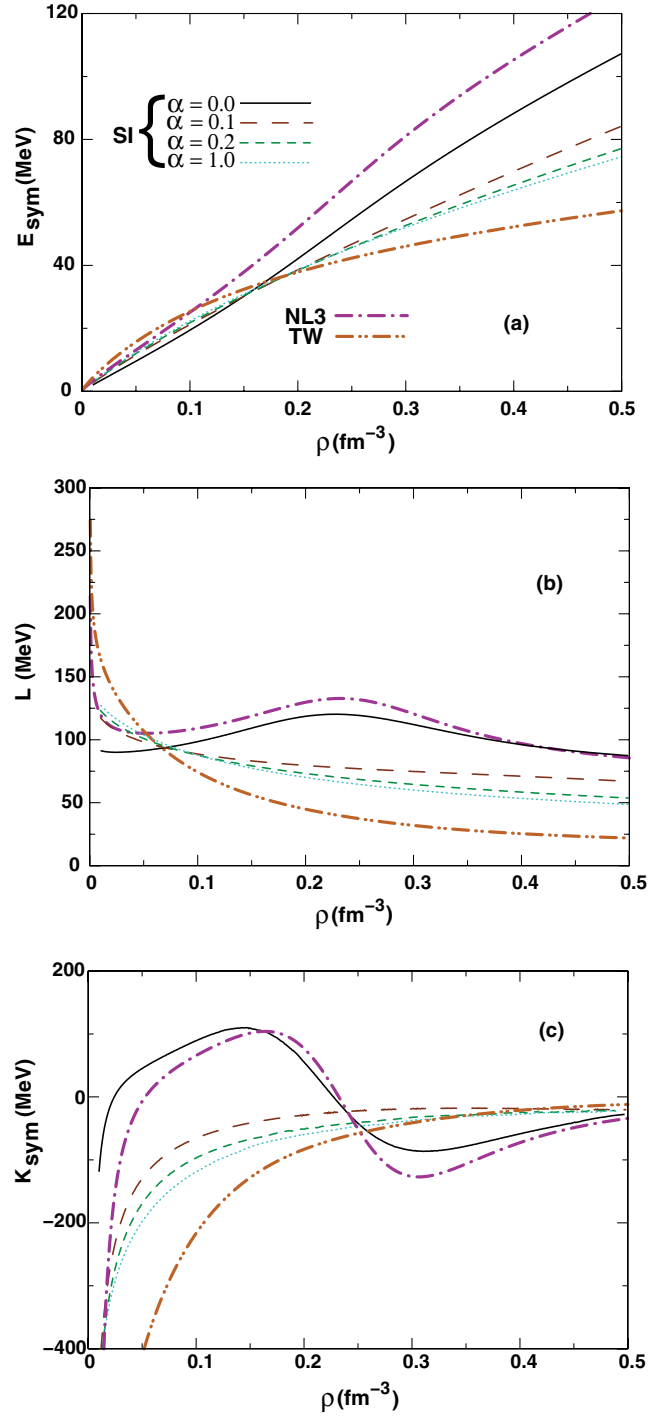

FIG. 4. (Color online) (a) Symmetry energy, (b) symmetry energy slope L, and (c) incompressibility $K_{\rm sym}$ for model SI with $\alpha = 0, 0.10, 0.20$, and $1.00 = \gamma$, $\beta = 0$. $\alpha = 0$ (solid line), $\alpha = 0.1$ [(dark-brown) long-dashed line], $\alpha = 0.2$ [(green) short-dashed line], $\alpha = 1.0$ [(cian) dotted line], NL3 [(purple) dot-dashed line], and TW [(light-brown dot-dot-dashed line].

onset density of strangeness ρ_s, the onset density of muons ρ_μ, the threshold density for the direct Urca process $\rho_{\rm DU}$ and the mass of a star with central density equal to $\rho_{\rm DU}$, $M_{\rm DU}/M_\odot$, and the mass $M_{\rm MAX}/M_\odot$ and radius of the stable star configuration with maximum mass.

TABLE I. Results for model S. The binding energy (15.75 MeV), saturation density (0.16 fm^{-3}), and symmetry energy (32.5 MeV) at saturation are the same for all parametrizations. Quantities given are the symmetry energy slope L, the symmetry energy incompressibility $K_{\rm sym}$, the symmetry term of the incompressibility of the nuclear EOS K_τ, the effective nucleon mass at saturation density M^*/M, the onset density of strangeness ρ_s, the onset density of muons ρ_μ, the threshold density for the direct Urca process $\rho_{\rm DU}$ and the mass of a star with central density equal to $\rho_{\rm DU}$, $M_{DU}/M_\odot$, and the mass $M_{\rm MAX}/M_\odot$ and radius of the stable star configuration with maximum mass.

α	L (MeV)	$K_{\rm sym}$ (MeV)	K (MeV)	K_τ (MeV)	Q_0 (MeV)	M^*/M	ρ_t (fm^{-3})	ρ_s (fm^{-3})	ρ_μ (fm^{-3})	$\rho_{\rm DU}$ (fm^{-3})	$M_{\rm DU}$ ($M_\odot$)	$M_{\rm MAX}$ ($M_\odot$)	R (km)
0.00	111.42	105.67	566	−970	−2068.27	0.537	0.1025	0.244	0.109	0.194	0.77	2.58	12.61
0.05	101.35	35.74	310	−601	−87.60	0.650	0.0969	0.282	0.109	0.210	0.71	2.11	10.68
0.10	98.22	13.39	224	−490	195.97	0.737	0.0952	0.309	0.110	0.221	0.68	1.79	9.50
0.20	96.60	2.55	212	−336	529.01	0.798	0.0950	0.330	0.111	0.229	0.68	1.54	9.31
0.40	95.92	−2.15	218	−312	603.79	0.833	0.0951	0.339	0.111	0.234	0.68	1.48	9.58
1.00	95.57	−3.95	224	−310	626.67	0.850	0.0951	0.345	0.112	0.236	0.68	1.49	9.91

TABLE II. The same as Table I for model SI.

α	L (MeV)	$K_{\rm sym}$ (MeV)	K (MeV)	K_τ (MeV)	Q_0 (MeV)	M^*/M	ρ_t (fm^{-3})	ρ_s (fm^{-3})	ρ_μ (fm^{-3})	$\rho_{\rm DU}$ (fm^{-3})	$M_{\rm DU}$ ($M_\odot$)	$M_{\rm MAX}$ ($M_\odot$)	R (km)
0.00	111.42	105.67	566	−970	−2068.27	0.537	0.1025	0.244	0.109	0.194	0.77	2.58	12.61
0.05	90.00	1.05	310	−564	−86.28	0.650	0.0970	0.284	0.107	0.213	0.69	2.11	10.69
0.10	82.34	−38.77	224	−402	355.86	0.737	0.0954	0.314	0.107	0.229	0.65	1.80	9.50
0.20	77.90	−64.01	212	−340	520.91	0.798	0.0952	0.339	0.107	0.248	0.65	1.55	9.26
0.40	76.25	−74.09	218	−323	596.36	0.833	0.0952	0.354	0.106	0.264	0.67	1.48	9.44
1.00	75.78	−78.79	224	−322	625.09	0.850	0.0954	0.366	0.106	0.278	0.69	1.49	9.53

TABLE III. The same as Table I for model SV.

α	L (MeV)	$K_{\rm sym}$ (MeV)	K (MeV)	K_τ (MeV)	Q_0 (MeV)	M^*/M	ρ_t (fm^{-3})	ρ_s (fm^{-3})	ρ_μ (fm^{-3})	$\rho_{\rm DU}$ (fm^{-3})	$M_{\rm DU}$ ($M_\odot$)	$M_{\rm MAX}$ ($M_\odot$)	R (km)
0.00	111.42	105.67	566	−970	−2068.27	0.537	0.1025	0.244	0.109	0.194	0.77	2.58	12.61
0.05	108.29	83.26	458	−848	−1190.65	0.554	0.0938	0.254	0.108	0.197	0.77	2.42	11.96
0.10	105.84	63.78	360	−751	−611.36	0.570	0.0861	0.263	0.108	0.199	0.73	2.26	11.31
0.20	102.40	36.71	276	−560	47.68	0.600	0.0793	0.281	0.108	0.204	0.69	1.96	10.06
0.40	99.00	12.42	195	−336	483.72	0.649	0.0727	0.310	0.108	0.212	0.63	1.39	8.70
1.00	96.66	−1.99	159	−165	685.86	0.710	0.0699	0.342	0.109	0.221	0.62	0.83	9.00

TABLE IV. The same as Table I for model SVI.

α	L (MeV)	$K_{\rm sym}$ (MeV)	K (MeV)	K_τ (MeV)	Q_0 (MeV)	M^*/M	ρ_t (fm^{-3})	ρ_s (fm^{-3})	ρ_μ (fm^{-3})	$\rho_{\rm DU}$ (fm^{-3})	$M_{\rm DU}$ ($M_\odot$)	$M_{\rm MAX}$ ($M_\odot$)	R (km)
0.00	111.42	105.67	566	−970	−2068.27	0.537	0.1025	0.244	0.109	0.194	0.77	2.58	12.61
0.05	98.18	45.03	458	−562	−83.73	0.554	0.0940	0.254	0.106	0.198	0.75	2.42	11.96
0.10	88.05	−0.74	360	−443	351.78	0.570	0.0863	0.265	0.105	0.203	0.68	2.26	11.31
0.20	74.84	−57.56	276	−364	525.89	0.600	0.0795	0.286	0.102	0.214	0.64	1.97	10.07
0.40	64.58	−98.07	195	−286	602.54	0.649	0.0731	0.323	0.100	0.239	0.59	1.40	8.65
1.00	61.13	−104.91	159	−231	626.04	0.710	0.0704	0.374	0.098	0.293	0.57	0.66	8.67

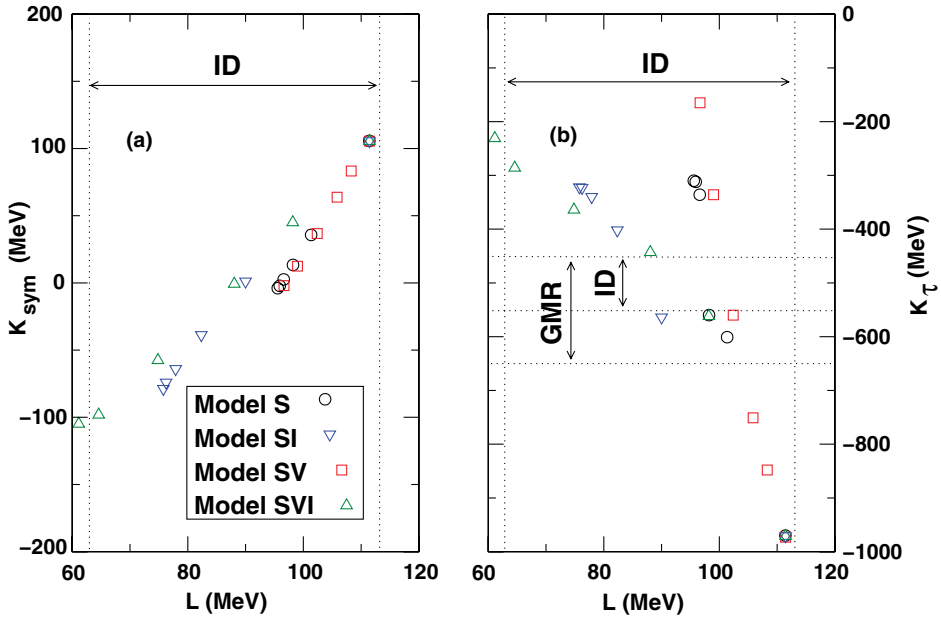

FIG. 5. (Color online) $K_{\rm sym}$ and K_τ as a function of the symmetry energy slope L for all parametrizations studied. Presently accepted limits from isospin diffusion (ID) in heavy-ion collisions [16,18], giant monopole resonance (GMR) in Sn isotopes [25,26], and neutron skin studies (NS) [19].

The slope L is within the experimental constraints 55 MeV $< L <$ 113 MeV for all parametrizations considered. In the S and SV models the value of the slope is quite large, though never below 95 MeV. The variation of L as the free parameter α increases is shown in Fig. 3. It is shown that L decreases with the increase in α, starting at ∼110 MeV and stabilizing at ∼95 MeV for models S and SV, at ∼75 MeV for model SI, and at ∼60 MeV for model SVI.

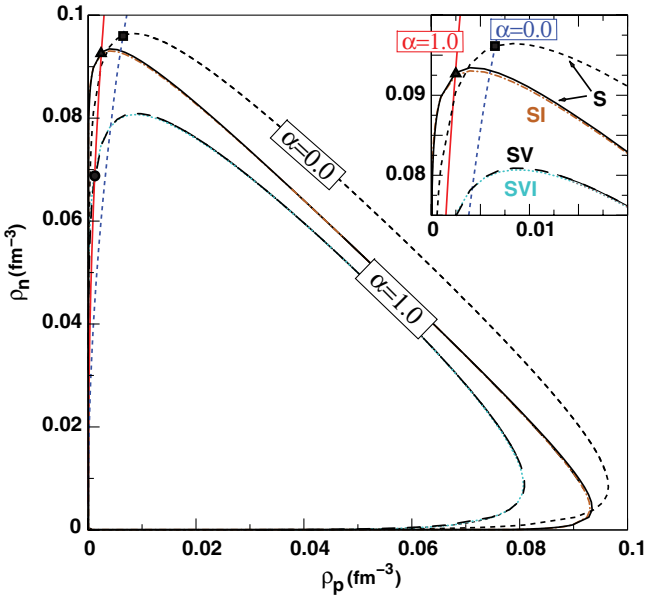

FIG. 6. (Color online) Spinodal curves for model S, $\alpha = 0$ (short-dashed line), models S and SI, $\alpha = 1$ (solid black and brown dot-dashed lines), and models SV and SVI, $\alpha = 1$ (long-dashed and cyan dotted lines), as indicated. The solid red, dot-dashed, and dark-blue dotted lines represent the β-equilibrium EOS for $\alpha = \beta = \gamma = 1$ (red line) and $\alpha = \beta = \gamma = 0$ (blue line), and the circle, triangle, and square stress the crossing point of the EOS with the spinodal for their respective α values. The inset magnifies the crossing of the β-equilibrium EOS with the spinodal.

A value of K_τ in the interval $[-400, -675]$ MeV imposes very strong restrictions. According to some authors [22,32,33], however, it is difficult to determine the experimental value of K_τ accurately, as it may suffer from the same ambiguities already encountered in earlier attempts to extract the incompressibility coefficient of infinite nuclear matter from finite-nucleus extrapolations. We, therefore, do not rule out models with values of K_τ larger than -400 MeV. In fact, in Ref. [24] the properties of several relativistic and Skyrme models that reproduce the ground-state properties of stable and unstable nuclei or the properties of nuclear or neutron matter have been compared, and it is shown that a large number of models have $K_\tau < -400$ MeV.

For reference, in Fig. 4 we plot, for the different parametrizations considered, the symmetry energy [Fig. 4(a)], its slope L [Fig. 4(b)], and the incompressibility $K_{\rm sym}$ [Fig. 4(c)] for model SI. We also include the corresponding curves obtained with the nonlinear Walecka model parametrization NL3 [34] and density-dependent relativistic hadronic model TW [30]. Varying α and γ between 0 and 1, we go from the hard symmetry energy behavior of NL3 to the soft TW behavior. Similar conclusions are madfe for the slope and the incompressibility: as we increase α the behavior of our parametric model changes from an NL3-like to a TW-like behavior.

To compare the predictions of the different parametrizations under study and the experimental constraints on L and K_τ, in Fig. 5 we plot $K_{\rm sym}$ and K_τ versus the slope L for all models. It is shown that $K_{\rm sym}$ and K_τ exhibit a linear correlation with L, as also discussed in Ref. [24]. We have checked that in fact this correlation also exists for the ratio Q_0/K, which enters the definition of K_τ. We include the constraints obtained from isospin diffusion (ID) in HICs [16,18], isotopic behavior of the giant monopole resonance (GMR) in Sn isotopes [25,26], and neutron skin studies (NS) [19]. The models that better satisfy the constraints are S and SI, with $0.05 < \alpha < 0.1$ and SVI, with $0.05 < \alpha < 0.2$. Model SV presents values with good

agreement with L and K_τ only for $\alpha \sim 0.2$. So far we have considered the S, SV, SI, and SVI versions of the PCM in which two, one, or none of the parameters has been set to zero, while the remaining parameters have been set equal. In the next sections we maintain this analysis to impose some constraints on the parameter choice, using neutron star observations. We finally vary the parameters independently and choose two sets that give excellent values not only for L and K_τ but also for K and neutron star maximum masses.

IV. THERMODYNAMICAL INSTABILITIES

The system is unstable against phase separation keeping volume and temperature constant, if the free energy curvature matrix $\mathcal{F}_{ij}$,

$$\mathcal{F}_{ij} = \left(\frac{\partial^2 \mathcal{F}}{\partial\rho_i \partial\rho_j}\right)_T, \tag{4}$$

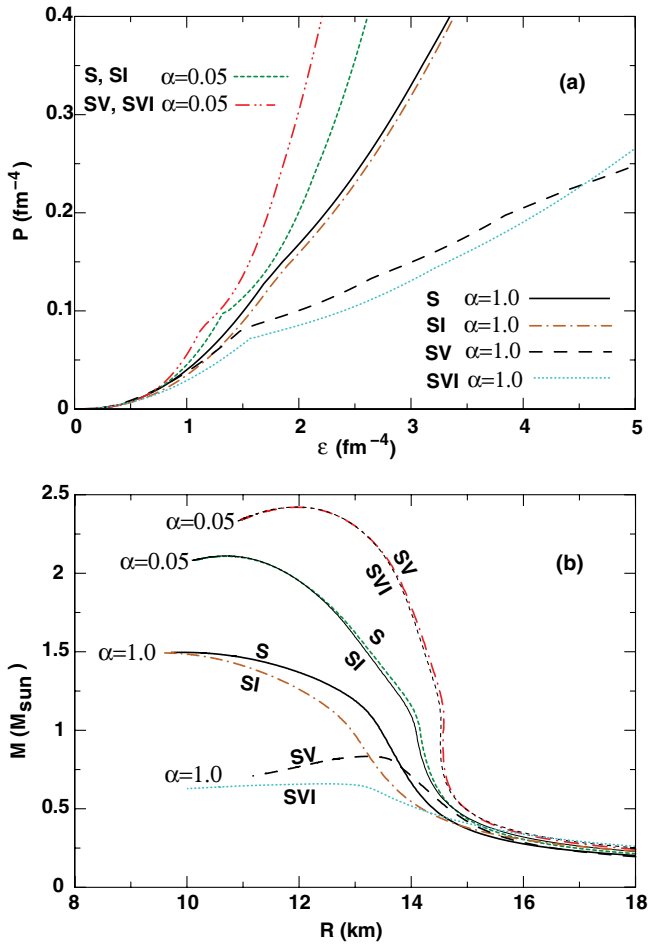

FIG. 7. (Color online) (a) Equation of state and (b) corresponding mass-radius curves for the families of stars obtained with the parametrizations in Tables I–IV. As indicated for $\alpha = 0.05$ the coincident S and SI curves are shown by the (green) short-dashed line, whereas the (red) dot-dot-dashed line stands represents the SV/SVI single curve. For $\alpha = 1.0$, the S, SI, SV, and SVI curves are shown by the (black) solid, (brown) dot-dashed, long-dashed, and (cyan) dotted lines, respectively.

is negative [35]. Stability implies that the free energy density $\mathcal{F}$ is a convex function of the densities ρ_p and ρ_n. In this section, we define the free energy $\mathcal{F}$ with no leptons or hyperons.

Because we are interested in studying the spinodal curve of the two-fluid nuclear system, it is enough to evaluate the zero of the smallest eigenvalue λ_- of $\mathcal{F}_{ij}$, where

$$\lambda_- = \frac{1}{2}[\mathrm{Tr}(\mathcal{F}) \pm \sqrt{\mathrm{Tr}(\mathcal{F})^2 - 4\mathrm{Det}(\mathcal{F})}]$$

and where the relevant eigenvectors are

$$\frac{\delta\rho_j{}^-}{\delta\rho_i{}^-} = \frac{\lambda_- - \mathcal{F}_{ii}}{\mathcal{F}_{ij}},$$

with $i, j = p, n$ [35,36].

The thermodynamic spinodal, defined by the $\lambda_- = 0$ condition, determines the instability regions of the system and is plotted in Fig. 6 for the models under discussion. We point out that, for symmetric matter, all the models have the same density, binding energy, and symmetry energy at saturation but different incompressibilities and effective nucleon masses. The model with the largest incompressibility (S; $\alpha = 0$) has the largest spinodal and the models with the smallest incompressibility (SV and SVI; $\alpha = 1$) have the smallest spinodal. The point of the spinodal with $\rho_p = \rho_n$ corresponds to the minimum of the pressure of symmetric nuclear matter, when the incompressibility is zero. Because we impose that the pressure is zero for all models at the same density, and the saturation density is 0.16 fm^{-3}, the incompressibility of the models with a larger curvature will become zero at a larger density. We note that the effect of the parameter γ is very small and seen only for very asymmetric matter, where it slightly reduces the spinodal.

In Fig. 6 we also plot the β-equilibrium EOS for $\alpha = 0$ and for model SVI with $\alpha = 1$. The crossing of the β-equilibrium EOS with the thermodynamical spinodal instability line gives a prediction for the transition density approximately 15% larger than the value obtained from a Thomas-Fermi calculation of the pasta phase [37]. Therefore, we determine the crust-core transition density from the crossing between the EOS and the

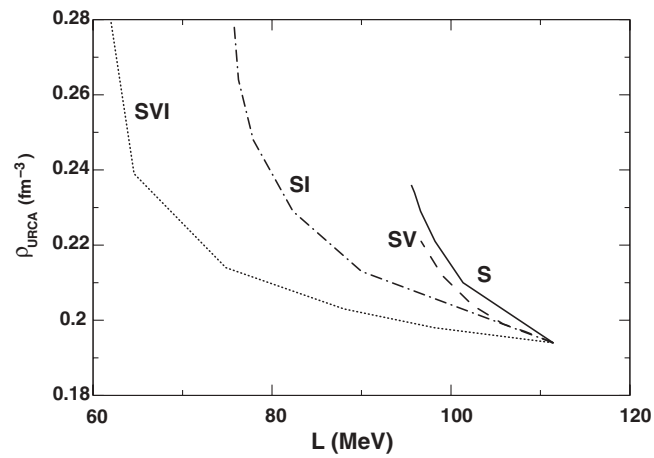

FIG. 8. Threshold density for the direct Urca process to occur versus the slope L. The dotted, dot-dashed, dashed, and solid lines represent models SVI, SI, SV, and S, respectively.

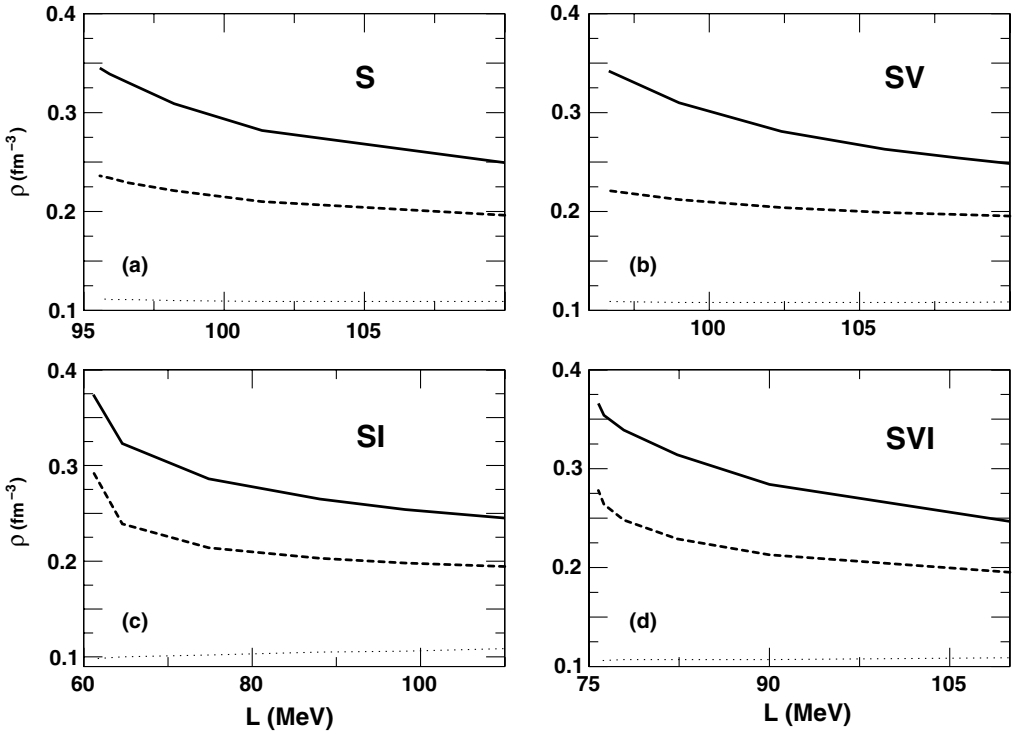

FIG. 9. Density for the strangeness (solid line), the Urca process (dotted line), and the muon (dashed line) onset for each version of the model.

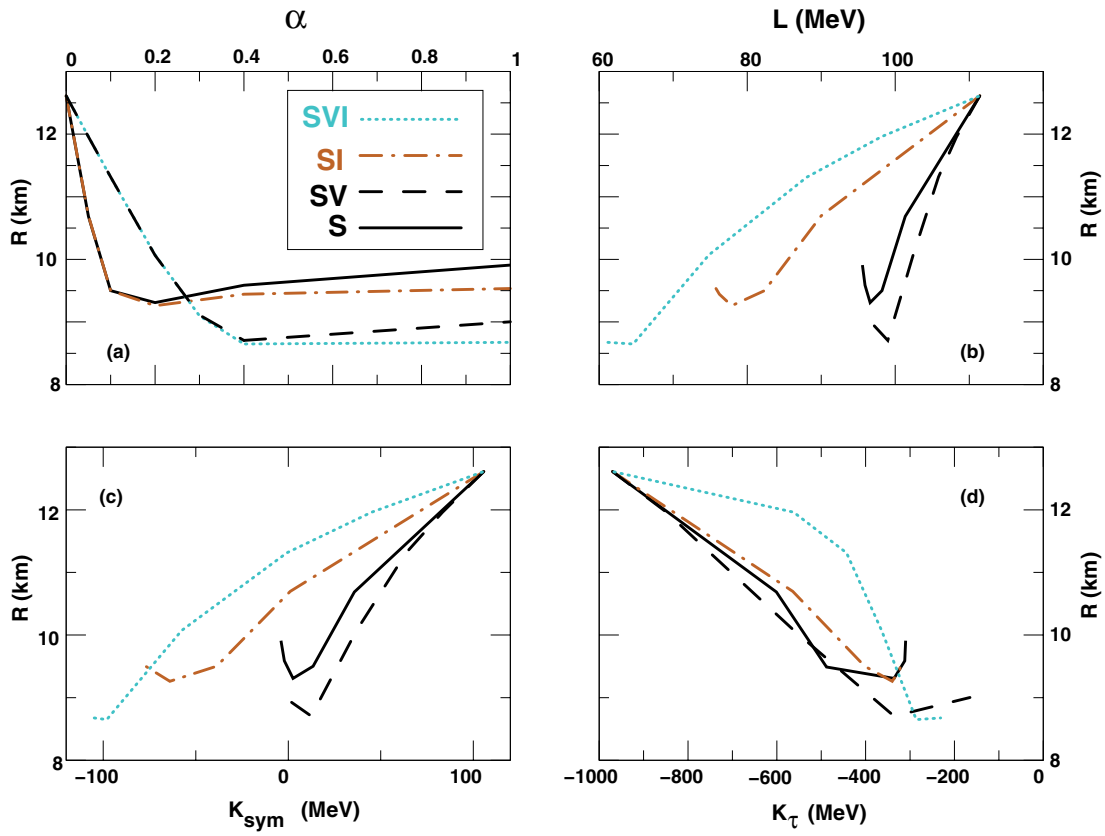

FIG. 10. (Color online) Radius of a star with maximum mass versus α, L, $K_{\rm sym}$, and K_τ, for the four versions of the PCM: models S (solid line), SI [(brown) dot-dashed line], SV (dashed line), and SVI [(cyan) dotted line].

TABLE V. Results for $\alpha = 0.1$ and $\beta = 0$.

γ	M^*/M	K (MeV)	L (MeV)	$K_{\rm sym}$ (MeV)	K_τ (MeV)	Q_0 (MeV)	ρ_t (fm^{-3})	ρ_s (fm^{-3})	ρ_μ (fm^{-3})	$\rho_{\rm DU}$ (fm^{-3})	$M_{\rm DU}$ ($M_\odot$)	$M_{\rm MAX}$ ($M_\odot$)	R (km)
0.450	0.749	224	60	−123.5	−585	−378.93	0.0894	0.305	0.107	0.253	0.68	1.811	9.512
0.240	0.749	224	70	−87.7	−587	−253.76	0.0874	0.305	0.107	0.240	0.67	1.806	9.510
0.120	0.749	224	80	−46.3	−583	−158.76	0.0865	0.305	0.107	0.231	0.66	1.803	9.511

spinodal and expect that our estimation of the transition density will define an upper bound of the correct transition density [38] between the crust and the core of a neutron star. It is shown that quite different predictions are obtained within the PCM for the transition density, both because the spinodals have a different behavior for neutron-rich matter and because the EOS for β-equilibrium stellar matter also differ when varying α from 0 to 1. Even if the EOS do not differ considerably for different parameters, the values of the density and isospin asymmetries at the crossing of the EOS with the spinodal are found to be quite different, though always with low proton densities. In Fig. 6 we only plot the EOS for $\alpha = 0$ and $\alpha = 1$ for model SVI. For the transition densities we have obtained 0.102 fm^{-3} ($\alpha = 0$), $\rho_t \sim 0.095$ fm^{-3} (models S and SI with $\alpha = 1$), and $\rho_t \sim 0.070$ fm^{-3} (models SV and SVI with $\alpha = 1$). The values of ρ_t given in Tables I–IV show a decrease in ρ_t with the decrease in the slope L, contrary to the results in Ref. [24]. However, we must take these values cautiously because we are varying not only the slope L, but also the incompressibility K, while imposing the same saturation density for all models. As a consequence the extension of the spinodal region grows with K and it is this correlation that is reflected in the data in Tables I–IV. In Sec. V we calculate the transition density for a selected set of parameters and then we will be able to obtain a correlation btween L and ρ_t similar to the one obtained in Ref. [24].

V. NEUTRON STAR CONSTRAINTS

Besides heavy-ion experiments, we can make use of astrophysical observations of neutron stars to establish some constraints on the PCM and its free parameters. We therefore obtain the EOS of β-equilibrium matter, including the presence of hyperons, and integrate the Tolman-Oppenheimer-Volkoff equation for a spherical compact star in hydrostatic equilibrium [39,40] to obtain the family of stars that correspond to each parametrization considered.

The different EOS are shown in Fig. 7(a) for all four versions of the model, considering the limiting values $\alpha = 0.05$ and $\alpha = 1.00$. The results for values of $0.05 < \alpha < 1.00$ are intermediate and lie between the two curves. The kink in each curve corresponds to the onset of strangeness. For $\alpha = 0.05$ the incompressibility is 310 MeV for models S and SI and 458 MeV for models SV and SVI. The last EOS is the hardest one, and therefore, the onset of hyperons occurs at smaller densities for this model. The hyperons make the EOS softer but never softer than any of the other versions (with higher values of α) of the model.

The corresponding neutron star families (mass-radius) are shown in Fig.7(b). As expected, one can see that all models with low values of α have maximum neutron star masses above $2M_\odot$, while the results change drastically when values of α approach the unit, reducing the maximum neutron star mass obtained with models S and SI to values close to $1.5M_\odot$. The results get even smaller when models SV and SVI are considered, reducing the maximum neutron star mass to values below $1M_\odot$.

One can establish the minimum value required for the maximum neutron star mass from observations. From Tables I–IV we see that, for models S and SI, which present almost the same neutron star masses, $\alpha < 0.1$ allows neutron star masses greater than $1.8M_\odot$, while models SV and SVI have a wider range of values ($\alpha < 0.3$) that yield the same star mass.

According to Ref. [41], observations on cooling predict that direct Urca should occur only in stars with a mass $M > 1.35M_\odot$. We have determined the star with maximum mass that does not allow the direct Urca process ($M_{\rm DU}$) for the different parametrizations of the model proposed. By $\rho_{\rm DU}$ we denote the baryonic density that defines the onset of the Urca process. The results are summarized in Tables I–IV. No model satisfies the condition $M_{\rm DU} > 1.35M_\odot$. All four versions of the model predict the Urca process with densities 0.194 fm$^{-3} < \rho_{\rm DU} < 0.293$ fm^{-3}, which correspond to neutron stars masses around $0.57\,M_\odot < M_{\rm DU} < 0.77\,M_\odot$. This result is expected, as PCM presents the same main features as the models discussed in Ref. [41], which are not in agreement with Urca expectations. The threshold density for the direct Urca process is plotted versus the slope L in Fig. 8. It is shown that it depends strongly on the slope of the symmetry energy: a smaller slope corresponds to a larger density of the Urca onset.

TABLE VI. Results for $\alpha = \beta = 0.2$.

γ	M^*/M	K (MeV)	L (MeV)	$K_{\rm sym}$ (MeV)	K_τ (MeV)	Q_0 (MeV)	ρ_t (fm^{-3})	ρ_s (fm^{-3})	ρ_μ (fm^{-3})	$\rho_{\rm DU}$ (fm^{-3})	$M_{\rm DU}$ ($M_\odot$)	$M_{\rm MAX}$ ($M_\odot$)	R (km)
0.310	0.60	276	60	−82.2	−517	−344.08	0.0884	0.286	0.102	0.218	0.65	1.971	10.072
0.210	0.60	276	70	−57.3	−539	−243.27	0.0877	0.286	0.102	0.214	0.64	1.968	10.077
0.125	0.60	276	80	−28.5	−547	−132.82	0.0868	0.286	0.102	0.210	0.63	1.966	10.069

TABLE VII. Results for TW and NL3.

Model	B/A (MeV)	ρ_0 (fm^{-3})	K (MeV)	M^*/M	$\mathcal{E}_{\rm sym}$ (MeV)	L (MeV)	$K_{\rm sym}$ (MeV)	K_τ (MeV)	ρ_t (fm^{-3})	ρ_s (fm^{-3})	ρ_μ (fm^{-3})	$\rho_{\rm DU}$ (fm^{-3})	$M_{\rm DU}$ ($M_\odot$)	$M_{\rm MAX}$ ($M_\odot$)	R (km)
TW	16.3	0.153	240.1	0.56	32.0	55.3	−124.7	−332.1	0.085	0.287	0.115	0.315	1.46	2.012	11.60
NL3	16.3	0.148	270	0.60	37.4	118.5	100.9	−698.4	0.065	0.217	0.111	0.205	1.00	1.707	12.65

We expect to be able to infer isospin asymmetry properties or establish a few constraints on the parametrizations from neutron star observations. Comparing models S and SI or models SV and SVI, which present the same global behavior, we identified a small difference in neutron star radii that becomes larger as α increases. For models S and SI the difference between the radii reaches $\Delta R = 380$ m for $\alpha = 1.0$, while it reaches $\Delta R = 330$ m for models SV and SVI. This difference would correspond, for example, to a difference of $\Delta\nu_f \sim 0.1$ kHz ($\sim$4%) in the fundamental mode of a star [42,43] and is larger if we consider stars with masses below the maximum allowed mass.

In Fig. 9 several properties of the neutron star structure are plotted as a function of the symmetry energy slope for models S, SV, SI, and SVI. The figure shows the baryonic densities at the onset of hyperons for each model. Hyperons are very important because their appearance results in softening of the EOS and lowering of the neutron star maximum mass. Figure 9 also presents the baryonic density at the muon onset and the density at which the proton fraction reaches the value that allows the direct Urca process to occur in neutron stars (for details see Refs. [29] and [41]). While the muon onset is not very sensitive to the value of L, the hyperon onset may vary by 40%–50%, and the densities for the onset of Urca by 20%–50%, between the limits of the plotted values of L, which are all within the experimental constrained values.

In Fig. 10 we analyze the dependence of the maximum-mass neutron star radius on α and the asymmetry parameters L, $K_{\rm sym}$, and K_τ. It is shown that there is a correlation that may help to impose restrictions on the parameters: smaller values of L, $K_{\rm sym}$, and $|K_\tau|$ give a larger radius for the maximum-mass configuration.

We propose to use the new parametrizations SI2 and SVI2 because models S, SI, SV, and SVI with reasonable incompressibilities predict maximum star masses that are too small. With a fixed α and/or $\alpha = \beta$ parameter and a changing γ parameter, we have changed the symmetry energy slope. Tables V and VI report the properties of the EOS and neutron stars for these new parametrizations. The maximum star masses have improved and are of the order $1.8M_\odot$, while the properties of symmetric nuclear matter are all reasonable. However, the density for Urca onset is still too small in all models and the radius of the maximum mass configuration is also quite small. We tried to vary all the parameters independently of each other but we were not able to find a parametrization that predicts larger densities for the onset of the Urca process than those already obtained. This seems to be a weak point of these models. We also made an estimation of the crust-core transition densities by calculating the crossing of the β-equilibrium EOS with the thermodynamical spinodal as explained in Sec. IV. The results are reported in Tables V and VI and vary between 0.086 and 0.089 fm^{-3}, showing a small decrease when the slope of the symmetry energy increases.

We next compare our results with two relative mean field models: NL3 with constant couplings and TW with density-dependent coupling parameters (Table VII). We have obtained better values for the slope of the symmetry energy for models SI2 and SVI2, well within the experimental range, than with NL3 and TW. For these two models the slope of the symmetry energy corresponds, respectively, to the upper and lower limit of L proposed from the experimental values. We have also obtained results for K_τ closer to the experimental ones than those found within NL3 and TW, maintaining good results for the compression modulus, effective nucleon mass, and neutron star global properties. The PCM introduces a density dependence on the coupling parameters weaker than the one with TW (see Fig. 2), mainly for the isospin channel. The parametrization of the coupling parameters within the PCM does not allow for such a strong density dependence for the coupling parameters as TW shows. For the crust-core transition density models SI2 and SVI2 preview a density similar to that obtained with TW. Concerning the correlation between ρ_t and L, models SI2 and SVI2 behave like those in Ref. [24], with the value of ρ_t decreasing as L increases. The density for the strangeness onset is closely related to the incompressibility of the EOS: SI2 is very soft and predicts the largest density for the strangeness onset; SVI2 gives a result very similar to that with TW, $\sim$40% larger than NL3. Other properties of models SI2 and SVI2 are also closer to TW than to NL3, except for the the onset density for the Urca process and the mass of the compact star with this density at the center: it is seen that, for other similar saturation properties, the value of K_τ for TW seems to be the only great difference.

VI. CONCLUSIONS

We have employed the parametric coupling model, developed by Taurines *et al.* [6], to describe nuclear matter properties, in particular, those related to the isospin channel, which had still not been investigated in the PCM. Some of the parameters of the model were fixed by the binding energy (15.75 MeV) and saturation density (0.16 fm^{-3}) for symmetric matter and by the symmetry energy (32.5 MeV). We have tried to restrict the remaining parameters by reproducing experimental results obtained with HICs at intermediate energies and neutron star properties.

Considering a wide range of experimental data for the slope of the symmetry energy L, 55 MeV $< L <$ 115 MeV, and for the symmetry term of the incompressibility of the nuclear EOS

K_τ, -375 MeV $< K_\tau < -650$ MeV, we have ruled out some values of the free parameters. The models that best satisfy the constraints are S and SI, with $0.05 < \alpha \lesssim 0.1$, and SVI, with $0.05 < \alpha \lesssim 0.2$. Model SV presents values with good agreement with the L and K_τ experimental values only for $0.2 \lesssim \alpha \lesssim 0.3$.

Some properties of neutron star matter and neutron star structure have been described with the PCM for the range of parameters restricted by the values of L and K_τ, namely, the maximum mass star configuration, and the densities of the onset of muons, strangeness, and the direct Urca process. It has been shown that all properties are reasonably well described except the prediction of the direct Urca process at a density that is too low. It is also shown that the density at the onset of muons is almost independent of the parameters of the model, but the strangeness onset is sensitive to the symmetry energy slope: a larger slope corresponds to a smaller onset density. The same is true for the direct Urca process, although with a slightly weaker dependence. It has also been shown that the radius and mass of the maximum-mass stable star configuration are correlated with the L value: a larger L corresponds to a larger radius and a larger mass. A similar correlation exists with the symmetry term of the incompressibility of nuclear matter. However, from model to model this correlation has a different slope and a given value of L and K_τ does not define the neutron star properties in a unique way.

Even though the proposed range of validity of the parameters of the PCM is in agreement with the experimental range described previously for heavy ions, it is a common belief that the slope of the symmetry energy should be close to the lower limit of the interval 55 MeV $< L <$ 115 MeV [19]. To investigate other possibilities of the model, we have proposed new parametrizations chosen to reproduce the symmetry energy slope $L = 60$, 70, and 80 MeV. These parametrizations have shown excellent results also for K_τ, K, M^*, and the neutron star maximum mass but still predict quite low densities for the onset of the Urca process. The results reported in Tables V and VI describe some of these results. We have tried to find a set of parameters that could predict a larger density for the onset of the direct Urca process, without success. The PCM presents the same main features of the models discussed in Ref. [41], which are not in agreement with Urca expectations.

We have constrained the free parameters of the PCM using the properties of asymmetric nuclear matter, but it is important to mention that the EOS that show the best results for these properties (see Tables V and VI) are in perfect agreement with those imposed by the analysis of symmetric nuclear matter properties such as those described in Ref. [44], where constraints, obtained from the analysis of nuclear matter flow in HICs, were proposed for the high-density EOS of symmetric matter. This problem was recently examined in Ref. [45]. It is also important to mention that the constraints imposed by asymmetric nuclear matter properties are stronger than those obtained from symmetric nuclear matter (for details see Ref. [45]).

We have compared our results with two relativistic mean field models: NL3 with constant couplings and TW with density-dependent coupling parameters (Table VII). It is shown that models SI2 and SVI2 predict results closer to those with TW except for the onset density of the Urca process. These could be related to the larger K_τ value that TW has, as all the other saturation properties are similar. It has also been shown that while the density dependence of the g_σ^* and g_ω^* coupling parameters in the PCM is similar to that with TW, the density dependence of g_ρ^* is very different.

The relation between the symmetry energy and some properties of neutron stars has also been discussed. The different models considered in the present study with one or more density-dependent couplings, showed quite large differences among them, even for the same values of L and K_τ. We conclude that the properties of nuclear matter for both symmetric and asymmetric matter at saturation are not enough to define the structure of compact stars and experimental data at two to three times saturation density are required.

ACKNOWLEDGMENTS

This work was partially supported by FEDER and FCT, under Project Nos. PTDC/FP/64707/2006, CERN/FP/83505/2008, and SFRH/BPD/29057/2006, and by COMPSTAR, an ESF Research Networking Programme.

[1] A. L. Fetter and J. D. Walecka, *Quantum Theory of Many-Particle Systems* (McGraw-Hill, New York, 1971).
[2] J. P. Blaizot, Phys. Rep. **64**, 171 (1980).
[3] J. Boguta and A. R. Bodmer, Nucl. Phys. **A292**, 413 (1977).
[4] J. D. Walecka, Ann. Phys. **83**, 491 (1974).
[5] J. Zimanyi and S. A. Moszkowski, Phys. Rev. C **42**, 1416 (1990).
[6] A. R. Taurines, C. A. Z. Vasconcellos, M. Malheiro, and M. Chiapparini, Phys. Rev. C **63**, 065801 (2001).
[7] A. Delfino, M. Chiapparini, M. Malheiro, L. Belvedere, and A. Gattone, Z. Phys. A **355**, 145 (1996).
[8] W. Koepf, M. M. Sharma, and P. Ring, Nucl. Phys. **A533**, 95 (1992).
[9] V. A. Dexheimer, C. A. Z. Vasconcellos, and B. E. J. Bodmann, Phys. Rev. C **77**, 065803 (2008).
[10] M. Razeira *et al.*, Int. J. Mod. Phys. E **16**, 2855 (2007).
[11] G. F. Marranghello, M. Razeira, B. E. J. Bodmann, and J. C. N. de Araujo, Int. J. Mod. Phys. E **16**, 2847 (2007).
[12] M. Grohmann *et al.*, Int. J. Mod. Phys. E **16**, 2838 (2007).
[13] B. A. Brown, Phys. Rev. Lett. **85**, 5296 (2000).
[14] S. Typel and B. A. Brown, Phys. Rev. C **64**, 027302 (2001).
[15] C. J. Horowitz and J. Piekarewicz, Phys. Rev. Lett. **86**, 5647 (2001).
[16] L. W. Chen, C. M. Ko, and B. A. Li, Phys. Rev. Lett. **94**, 032701 (2005); Phys. Rev. C **72**, 064309 (2005).
[17] A. W. Steiner, M. Prakash, J. Lattimer, and P. J. Ellis, Phys. Rep. **411**, 325 (2005).
[18] B. A. Li, L. W. Chen, and C. M. Ko, Phys. Rep. **464**, 113 (2008).
[19] M. Centelles, X. Roca-Maza, X. Viñas, and M. Warda, Phys. Rev. Lett. **102**, 122502 (2009).
[20] P. Danielewicz and J. Lee, Nucl. Phys. **A818**, 36 (2009).

[21] L. W. Chen, B. J. Cai, C. M. Ko, B. A. Li, C. Shen, and J. Xu, arXiv:0905.4323.
[22] J. Piekarewicz and M. Centelles, Phys. Rev. C **79**, 054311 (2009).
[23] J. Xu, L. W. Chen, B. A. Li, and H. R. Ma, Phys. Rev. C **79**, 035802 (2009).
[24] I. Vidaña, C. Providência, A. Polls, and A. Rios, Phys. Rev. C **80**, 045806 (2009).
[25] U. Garg *et al.*, Nucl. Phys. **788**, 36 (2007).
[26] T. Li, U. Garg, Y. Liu *et al.*, Phys. Rev. Lett. **99**, 162503 (2007).
[27] D. V. Shetty, S. J. Yennello, and G. A. Souliotis, Phys. Rev. C **76**, 024606 (2007).
[28] M. A. Famiano, T. Liu, W. G. Lynch *et al.*, Phys. Rev. Lett. **97**, 052701 (2006).
[29] J. M. Lattimer, C. J. Pethick, M. Prakash, and P. Haensel, Phys. Rev. Lett. **66**, 2701 (1991).
[30] S. Typel and H. H. Wolter, Nucl. Phys. **A656**, 331 (1999).
[31] G. Baym, C. Pethick, and P. Sutherland, Astrophys. J. **170**, 299 (1971).
[32] J. Piekarewicz, Phys. Rev. C **76**, 031301(R) (2007).
[33] H. Sagawa, S. Yoshida, G. M. Zeng, J. Z. Gu, and X. Z. Zhang, Phys. Rev. C **76**, 034327 (2007).
[34] G. A. Lalazissis, J. König, and P. Ring, Phys. Rev. C **55**, 540 (1997).
[35] J. Margueron and P. Chomaz, Phys. Rev. C **67**, 041602(R) (2003).
[36] S. S. Avancini, L. Brito, Ph. Chomaz, D. P. Menezes, and C. Providência, Phys. Rev. C **74**, 024317 (2006).
[37] S. S. Avancini, L. Brito, J. R. Marinelli, D. P. Menezes, M. M. W. Moraes, C. Providência, and A. M. Santos, Phys. Rev. C **79**, 035804 (2009).
[38] C. J. Pethick, D. G. Ravenhall, and C. P. Lorenz, Nucl. Phys. **A584**, 675 (1995).
[39] J. R. Oppenheimer and G. M. Volkoff, Phys. Rev. **55**, 374 (1939).
[40] R. C. Tolman, Phys. Rev. **55**, 364 (1939).
[41] T. Klähn, D. Blaschke, S. Typel *et al.*, Phys. Rev. C **74**, 035802 (2006).
[42] O. Benhar, V. Ferrari, and L. Gualtieri, Phys. Rev. D **70**, 124015 (2004).
[43] G. F. Marranghello and J. C. N. de Araujo, Class. Quant. Grav. **23**, 6345 (2006).
[44] P. Danielewicz, R. Lacey, and W. G. Lynch, Science **298**, 1592 (2002).
[45] G. F. Marranghello and C. A. Z. Vasconcellos, Int. J. Mod. Phys. E (in press).